

A New Determination of the (Z, A) Dependence of Coherent Muon-to-Electron Conversion

Léo Borrel, David G. Hitlin, and Sophie Middleton
California Institute of Technology
Pasadena, CA 91125 USA
(Dated: January 29, 2024)

Should muon-to-electron conversion in the field of a nucleus be found in the current generation of experiments, the measurement of the atomic number dependence of the process will become an important experimental goal. We present a new treatment of the (Z, A) dependence of coherent muon-to-electron conversion in 236 isotopes. Our approach differs from previous treatments in several ways. Firstly, we include the effect of permanent quadrupole deformation on the charged lepton flavor violating matrix elements, using the method of Barrett moments. This method also enables the addition of muonic X-ray nuclear size and shape determinations of the charge distribution to the electron scattering results used previously. Secondly, we employ a Hartree-Bogoliubov model to calculate neutron-related matrix elements for even-even nuclei. This takes into account the quadrupole deformation of the neutron distributions and the fact that neutrons are, in general, in different shell model orbits than protons. The calculated conversion rates differ from previous calculations, particularly in the region of large permanent quadrupole deformation. Finally, we propose an alternative normalization of the muon-to-electron conversion rate, which related more closely to what a given experiment actually measures, and better separate lepton physics from nuclear physics effects.

I. INTRODUCTION

The most stringent experimental upper limit on charged lepton flavor violation (CLFV) via muon-to-electron conversion ($\mu \rightarrow e$) in the field of a nucleus ($R_{\mu e} \leq 7 \times 10^{-13}$ at 90% C.L.) was set by the SINDRUM-II experiment using a gold target [1]. The Mu2e [2] and COMET [3] experiments, both nearing data-taking, will search for $\mu \rightarrow e$ using an aluminum target. The Mu2e experiment at Fermilab aims to reach a single event sensitivity (SES) of $\sim 3 \times 10^{-17}$ for the conversion rate relative to muon capture. The COMET experiment at J-PARC, has a planned sensitivity of 2×10^{-15} for Phase I and a similar sensitivity to Mu2e for Phase II [4]. CLFV limits derived from the decays $\mu^+ \rightarrow e^+ \gamma$ and $\mu^+ \rightarrow e^+ e^- e^+$, mainly sensitive to dipole coupling, provide comparable or better limits. The new generation of experiments, MEG-II for $\mu^+ \rightarrow e^+ \gamma$ [5] and Mu3e for $\mu^+ \rightarrow e^+ e^- e^+$ [6], are underway at PSI.

Should the decay or conversion experiments find evidence for CLFV decays or $\mu \rightarrow e$ conversion in aluminum, interest will turn to understanding the effective operators that mediate CLFV at low energies. This can be done by studying the Dalitz plot distributions of polarized muon or tau decays to three leptons [7–9] or by measurements of the conversion rate with other nuclear targets, as the (Z, A) dependence of the conversion rate can probe the Lorentz structure [10–12]. Future proposed experiments, such as Mu2e-II [13] and a conversion search at the Advanced Muon Facility [14], will provide opportunities to measure $\mu \rightarrow e$ conversion in other target materials.

The $\mu \rightarrow e$ conversion process manifestly involves the nuclear physics of the target elements. We discuss herein several aspects of extracting the New Physics from nuclear physics. In particular, we present a new systematic

study of the atomic number dependence of the coherent conversion rate. We utilize the method of Barrett moments [15] to add a substantial amount of muonic X-ray data to previous studies that mainly employ electron scattering data on nuclear charge distributions. This allows us to take into account the fact that many nuclei have permanent quadrupole deformations, which affects the evaluation of matrix elements of New Physics operators. We also employ a new treatment of the neutron distribution and present a new treatment of the normalization of experimental and theoretical results.

The study of the (Z, A) dependence of conversion is most cleanly done with a target consisting of a single stable isotope, as with $^{27}_{13}\text{Al}$, the target in both the Mu2e and COMET experiments. Potential higher Z targets such as Ti have many stable isotopes and are typically not readily available as separated isotopes in sufficient quantity to meet experimental conversion sensitivity requirements. Therefore, in Sec. III we discuss conversion rates for both targets composed of individual isotopes and targets with natural elemental abundance. Section IV addresses the question of the historical approach to the presentation of experimental limits on $\mu \rightarrow e$ conversion. The usual approach, in analogy to the concept of a decay branching fraction, is to normalize the conversion rate to the rate of muon capture on a particular nucleus, and therefore to present limits on this ratio, referred to as $R_{\mu e}$:

$$R_{\mu e}(A, Z) = \frac{\Gamma(\mu^- + N(A, Z) \rightarrow e^- + N(A, Z))}{\Gamma(\mu^- + N(A, Z) \rightarrow \text{all captures})}. \quad (1)$$

We introduce an alternative normalization, which hews more closely to what a given experiment actually measures and better separates the lepton physics and the nuclear physics, removing extraneous contributions to the Z, A dependence of conversion.

Section V is a discussion of the practicalities involved in choosing future targets.

II. REVIEW OF EXISTING LITERATURE

Should CLFV be observed in $\mu \rightarrow e$ conversion in the upcoming round of experiments, interest will turn to identifying the Lorentz structure of the CLFV coupling. This can be accessed by a sufficiently precise measurement of the atomic number dependence of the conversion rate [10–12, 16].

The most widely cited treatment of the atomic number dependence of coherent $\mu \rightarrow e$ conversion is that of Kitano, *et al.*[10], extended by Cirigliano *et al.*[11], which includes 55 isotopes whose charge distributions, measured using elastic electron scattering, were compiled by De Vries *et al.*[17]. These measurements are parameterized using a variety of models for the nuclear charge distribution: harmonic oscillator, two and three-parameter spherical Fermi, two and three-parameter Gaussian, as well as model-independent sum-of-Gaussians, and Fourier-Bessel expansion treatments where available. The spin-independent contribution to the coherent conversion rate has an A^2 enhancement and in most, but not all, models is dominant. Three types of effective operators, scalar, vector and dipole, contribute to coherent conversion. The rate of $\mu \rightarrow e$ conversion is calculated using the overlap integrals between the Dirac wave functions and nucleon densities for these three cases. While some direct measurements of neutron distributions are explored in Refs.[10, 11], for the main results the neutron and proton distributions are assumed to be identical and are scaled by N/Z .

The recent calculations of Haxton *et al.* [18] improve these analyses for a selected number of nuclei by employing nuclear-level effective field theory to determine the matrix elements. Effective field theory has also been exploited to refine the interpretation of experimental CLFV limits in terms of New Physics couplings [19].

The Kitano *et al.* and Cirigliano *et al.* studies present the Z -dependence of the conversion rates for 28 and 55 isotopes respectively, that have had their muon capture lifetime measured [20] in the form of a ratio: $R_{\mu e}(A, Z) = R_{\mu e}^Z/R_{\mu e}^{Al}$. This ratio has a great deal of structure, largely due to the influence of “magic numbers” associated with closed shells in the nuclear shell model on the nuclear size and shape. The influence of shell structure on the nuclear size, and thus the evaluation of the New Physics matrix elements for the largely coherent conversion process is unavoidable. The additional structure in the Z dependence, introduced by the division by the muon capture rate, a non-coherent Standard Model process, can, however, be avoided. This formulation is traceable in part to the original conversion normalization proposal of Weinberg and Feinberg [21]. The question of normalization of the conversion rate will be discussed in Section IV.

A. Treatment of the neutron distribution

Kitano *et al.* [10] used measured neutron distributions when possible. These measurements, derived from charged pion, proton or alpha particle scattering, were available for only 16 nuclei. Their primary method of including neutrons in determining the (Z, A) dependence of conversion was therefore to scale the proton distribution by a factor of N/Z . Particularly in heavy nuclei, protons and neutrons populate levels with different quantum numbers and are thus in different shells. This produces rather different shapes and sizes for protons and neutrons. In particular quadrupole deformations, as measured by B(E2) (the electric quadrupole transition probabilities) determined by Coulomb excitation and by muonic X-ray hyperfine structure, show a different dependence for protons and neutrons [22]. We have therefore resorted to a model calculation to account for these details. To improve on simple N/Z scaling, we account for the fact that neutron distributions are typically larger than proton distributions by using a comprehensive set of calculations employing a deformed relativistic Hartree-Bogoliubov model [23, 24] to estimate the size and shape of the neutron distributions. This approach more accurately accounts for the fact that in most nuclei, particularly those in the region of large permanent quadrupole deformation ($Z = 60-80$), neutrons are in different shells than protons. Zhang *et al.* [25] have developed a deformed relativistic Hartree-Bogoliubov model [23, 24] for even-even nuclei ranging from $Z = 8$ to $Z = 120$ to determine individual neutron and proton distributions, accounting for quadrupole deformation. This work is being extended to other nuclei [26], but is not yet comprehensive beyond the even-even-sector.

B. The effects of deformed nuclei

Many nuclei, especially those with protons or neutrons far from a closed shell, are non-spherical, having permanent quadrupole or higher multipole shapes. The question addressed herein is what is the effect of these deformations on the calculation of $\mu \rightarrow e$ conversion rates? The μ to e conversion occurs primarily from the $1S$ state, so one can calculate conversion rates using only the radial Dirac equation with an equivalent spherically symmetric charge (or neutron) distribution. However, characterizing the average over non-spherical distributions with a derived *rms* radius does not account for the effective smearing at the outer edge of a nucleus due to, for example, a quadrupole deformation.

The effective nuclear charge or neutron distribution skin thickness enters into the evaluation of the CLFV matrix elements. The relative importance of the skin thickness in determining the matrix element depends on the atomic number (*c.f.* N/Z) and the quadrupole deformation. We calculate the CLFV matrix elements using a Dirac equation with spherical symmetry, the angular

integration accounting for the effect of the quadrupole deformation, whether oblate or prolate. This produces an effect largely concentrated at the nuclear surface, increasing the effective skin thickness of the charge distribution. The N/Z ratio increases with atomic number; the excess neutrons producing a “neutron skin”, a larger effective skin thickness for the neutrons, as well as effects on the charge distribution, *e.g.* isotope shifts in electronic or muonic atom spectra. These effects are further modulated by both proton and neutron shell structure, particularly around magic number closed shells.

The case of ^{27}Al is of particular interest, as it is the target for the Mu2e and COMET experiments. ^{27}Al has a large quadrupole moment (0.146 be^2) [27]. Most shell model calculations conclude that this nucleus has a prolate shape, with $\beta = 0.39$, although Dehnhard [28] argues for an oblate ground state deformation. The sign of the quadrupole deformation does not enter into the calculation of the relevant integrals in the solution of the Dirac equation.

C. The isotopes of Neodymium

Neodymium has five significant stable isotopes whose charge distributions have been measured in both electron scattering [29] and muonic X-ray spectra [30]. This provides an opportunity to explore some of the subtleties encountered in combining these different determinations of the nuclear charge distribution. There are measurements on five even-even neodymium isotopes: $A=142$, 144, 146, 148, and 150, which range from spherical to deformed. This allows us to explore the interplay of the effect of a quadrupole deformation on the effective skin thickness, as well as the differences between the two techniques, as shown in Fig. 1.

The values of the quadrupole deformation β determined largely from $B(E2)$ measurements [22], show a steady increase with neutron number, culminating at $N = 90$ (plotted in Figure 2). The value of β in the three-parameter fits to the charge distribution is held fixed for both the muonic X-ray and electron scattering cases.

The calculations of Zhang *et al.* using a Hartree-Bogoliubov model show that the *rms* charge radius of these Nd isotopes grows as $A^{1/3}$, while the neutron radius grows more quickly, as the neutrons are in a higher shell and further from a shell closure. This is our primary motivation for using the Zhang *et al.* calculations in evaluating the $S(n)$ and $V(n)$ overlap integrals, rather than scaling the neutron distributions by N/Z as has heretofore been the practice [10][11]. Related calculations by the Zhang *et al.* nuclear theory group [26] also reproduce the behavior of the quadrupole deformation in the Nd isotopes as a function of neutron number.

D. Goal of this study

We present a new determination of the atomic number dependence of the coherent conversion rate, using the method of Barrett moments [15] to add the many muonic X-ray measurements of nuclear charge distributions to the electron scattering data used in previous studies. The muonic X-ray data encompass measurements of many strongly-deformed nuclei, using the resolved hyperfine structure in the X-ray transitions to measure the nuclear quadrupole moment shape, typically parameterized by a three-parameter Fermi distribution.

Our treatment of the A and Z dependence of conversion differs from previous treatments in several ways:

- While previous studies have mainly used electron-scattering-based nuclear size determinations, we include the many measurements of nuclear charge distributions determined using muonic X-rays. This substantially enlarges the sample size, particularly in the regime above $Z = 60$, where many nuclei have substantial quadrupole deformations. We combine the elastic electron scattering and muonic X-ray data using the method of Barrett moments, and devise a procedure to incorporate the effect of permanent Y_{20} deformations on the effective nuclear skin thickness. By this approach, we can include the conversion rates for a total of 236 isotopes.
- Rather than using a neutron distribution determined by scaling the proton charge distributions by N/Z , the primary method used in previous treatments, we use a deformed relativistic Hartree-Bogoliubov model [25] for the neutron distributions and compare with other approaches. This model, bench-marked against a wide variety of experimental determinations for even-even nuclei, allows us to include a wider variety of nuclei and to explore isotopic effects on the conversion rate.
- We present the $\mu \rightarrow e$ conversion rates for the coherent New Physics process normalized to the total muon lifetime, rather than to the muon capture rate.

III. ATOMIC NUMBER DEPENDENCE OF $\mu \rightarrow e$ CONVERSION

A. Theoretical background

In the following study we concentrate on the dominant spin-independent coherent conversion process in which the final and initial state of the nucleus is identical and the coherent conversion rate is enhanced by A^2 .

The lepton flavor-violating coherent conversion rate of a muon into an electron is given by Kitano *et al.* [10] as:

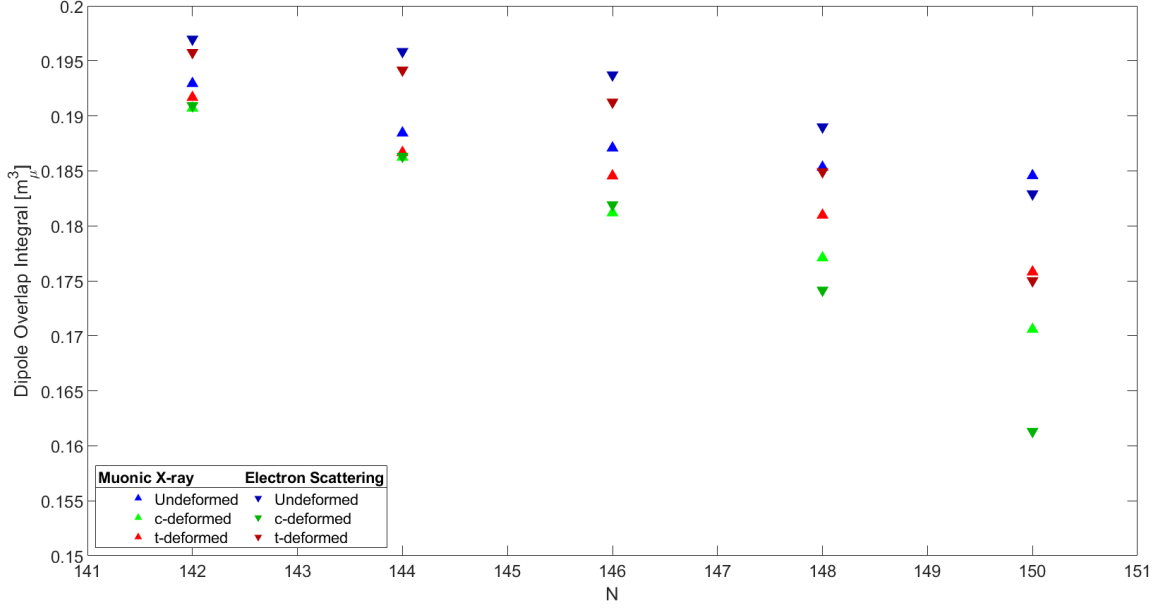


FIG. 1. The square of the dipole CLFV matrix element for five even-even isotopes of Nd as determined using muonic x-ray data [30] and electron scattering data [29] and three treatments of the charge distribution.

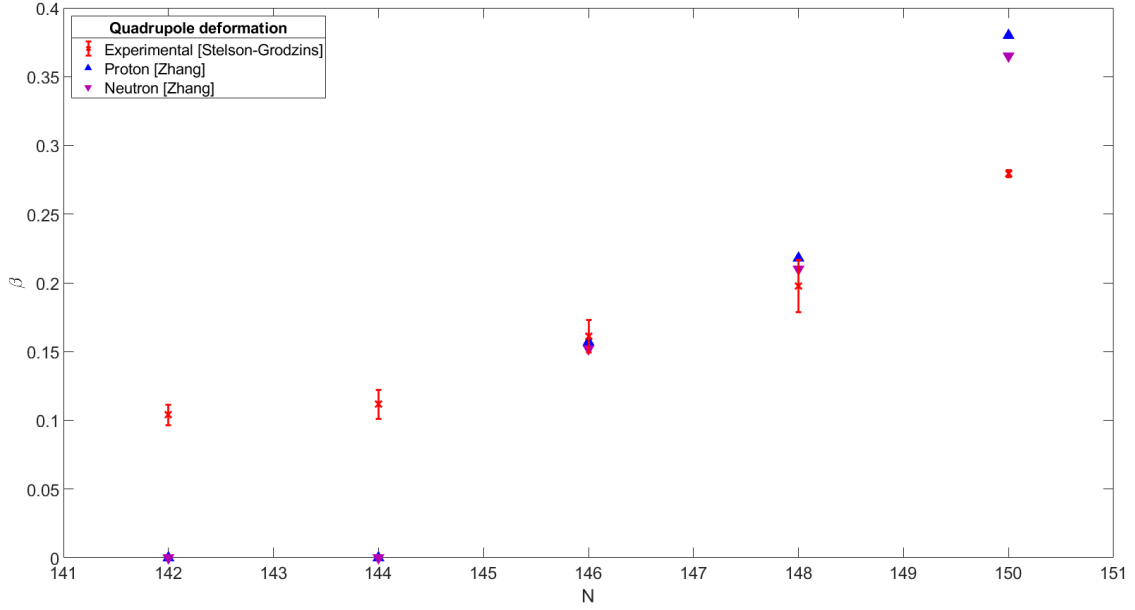


FIG. 2. Quadrupole deformation of five even-even isotopes of Nd determined from B(E2) measurements in Coulomb excitation [22] (with experimental uncertainty), and calculated for the charge and neutron distributions in the model of Zhang *et al.* [25].

$$\begin{aligned}
 \omega_{conv} = & 2G_f^2 \left| A_R^* D + \tilde{g}_{LS}^{(p)} S^{(p)} + \tilde{g}_{LS}^{(n)} S^{(n)} + \tilde{g}_{LV}^{(p)} V^{(p)} + \tilde{g}_{LV}^{(n)} S^{(n)} \right|^2 \\
 & + 2G_f^2 \left| A_L^* D + \tilde{g}_{RS}^{(p)} S^{(p)} + \tilde{g}_{RS}^{(n)} S^{(n)} + \tilde{g}_{RV}^{(p)} V^{(p)} + \tilde{g}_{RV}^{(n)} S^{(n)} \right|^2
 \end{aligned} \tag{2}$$

with G_F the Fermi constant, $A_{R,L}^*$ and \tilde{g} are dimensionless coupling constants describing the strength of each component of the Lagrangian and D , S and V represent overlap integrals for dipole, scalar, and vector interactions respectively. The L and R subscripts indicate left-handed and right-handed components and the (n) and (p) superscripts denote the neutron and proton terms respectively.

The overlap integrals are defined as:

$$\begin{aligned}
 D &= \frac{4}{\sqrt{2}} m_\mu \int_0^\infty (-E(r)) (g_e^- f_\mu^- + f_e^- g_\mu^-) r^2 dr \\
 S^{(p)} &= \frac{1}{2\sqrt{2}} \int_0^\infty Z \rho^{(p)}(r) (g_e^- g_\mu^- - f_e^- f_\mu^-) r^2 dr \\
 S^{(n)} &= \frac{1}{2\sqrt{2}} \int_0^\infty (A - Z) \rho^{(n)}(r) (g_e^- g_\mu^- - f_e^- f_\mu^-) r^2 dr \\
 V^{(p)} &= \frac{1}{2\sqrt{2}} \int_0^\infty Z \rho^{(p)}(r) (g_e^- g_\mu^- + f_e^- f_\mu^-) r^2 dr \\
 V^{(n)} &= \frac{1}{2\sqrt{2}} \int_0^\infty (A - Z) \rho^{(n)}(r) (g_e^- g_\mu^- + f_e^- f_\mu^-) r^2 dr
 \end{aligned}$$

where f and g are the large and small components of the radial solution of the Dirac equation describing a muon orbiting a nucleus and converting to an electron. The functions f_μ and (f_e) are the muon (electron) wavefunction [31]. The terms $\rho^{(n)}$ and $\rho^{(p)}$ describe the neutron and proton densities in the nuclei respectively. The electric field, $E(r)$, is fixed by Gauss' Law:

$$E(r) = \frac{Ze}{r^2} \int_0^r r'^2 \rho^{(p)}(r') dr'. \quad (3)$$

The muon and electron wavefunctions in the vicinity of the ^{27}Al nucleus are shown in Figure 3. The conversion occurs overwhelmingly from the $1S$ state; we therefore integrate over polar and azimuthal angles to account for the effect of quadrupole deformations.

B. Methodology

1. Combining electron scattering and muonic X-ray measurements

In order to combine measurements of nuclear charge distribution obtained by electron scattering and muonic X-rays we use the method developed by Barrett [15]. Electron scattering experiments derive information on the nuclear charge distribution from the energy and angular distribution of the scattered electron, mapping the momentum transfer of the electron to the Fourier transform of the charge distribution [17]. These treatments typically keep only the first term in the q^2 expansion. Muonic X-ray experiments use the energy of X-rays emitted in the atomic cascade of muonic atoms to determine

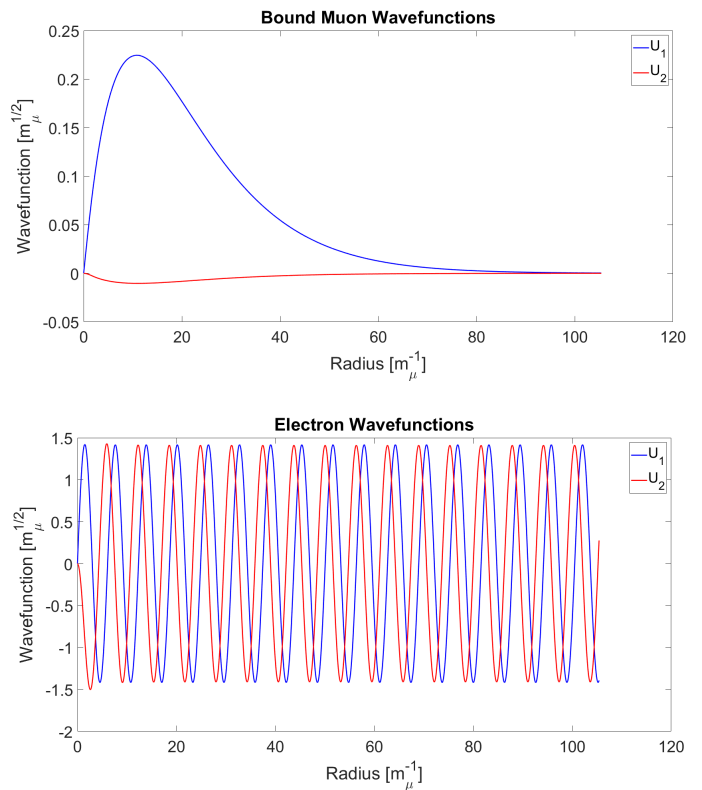


FIG. 3. The two components of the wavefunctions of the muon (top) and the electron (bottom) in the vicinity of the Al nucleus. Here $u_1 = r g_{e,\mu}^-$ and $u_2 = r f_{e,\mu}^-$.

the size and shape of the nucleus. Due to the strong overlap of the muon wavefunction with the nucleus, the energy of the $3D - 2P$ and $2P - 1S$ transitions is highly sensitive to nuclear size parameters. Analysis of the hyperfine structure allows the model-dependent determination of permanent quadrupole charge distributions.

While for light nuclei the $2P - 1S$ transition energy of a muonic atom can be matched to a single mean square radius $\langle r^2 \rangle$, this is not true for heavier nuclei, where nuclear distributions with the same RMS radius can generate quite different transition energies. Barrett [15] introduced a different moment, shared by all nuclear distributions yielding the same transition energy. The Barrett moment is defined as:

$$\langle r^k e^{-\alpha r} \rangle = \frac{4\pi}{Ze} \int \rho(r) r^k e^{-\alpha r} r^2 dr, \quad (4)$$

where k and α , which are Z -dependent, are given in [15].

In both electron scattering and muonic X-ray analyses, the nuclear charge distribution has often been described using a 2-parameter Fermi distribution (2pF):

$$\rho(r) = \frac{\rho_0}{1 + \exp\left[\frac{r-e}{t}\right]}, \quad (5)$$

where c is the radius at the half maximum and t is the skin thickness, defined as the region in which the charge density falls from 90% to 10% of the central value. This model is central to our Barrett moment-centered treatment.

We can see an example of the computation of the Barrett moment from two different datasets for Neodymium in Table I. The Barrett moments derived from the two types of experiments are seen to be in good agreement, supporting our approach to combining the electron scattering and muonic x-ray of measurements in determining the Z dependence of the conversion rate.

2. Quadrupole deformation

In order to compute the overlap integral, we need to solve the Dirac equation to obtain the muon and electron wavefunctions (as described in Section III A). We used an existing code [32] to solve the Dirac equation for a muonic atom in the potential of a spherically-symmetric 2-parameter Fermi distribution.

The method used to include the effect of nuclear quadrupole deformation on the matrix elements is as follows:

- employ a deformed 3-parameter Fermi distribution:

$$\rho(r, \theta) = \frac{\rho_0}{1 + \exp\left[\frac{r - c(1 + \beta Y_{20}(\theta))}{t}\right]} \quad (6)$$

where we take parameters c , t and β from available literature detailed in Section III B 3.

- We convert this to a spherically-symmetric 2-parameter Fermi distribution by removing the quadrupole deformation β and adjusting the skin thickness t to keep a constant Barrett moment (defined in equation 4). This equivalent 2-parameter Fermi distribution is then used to solve the Dirac equation.

Using the t parameter to match the Barrett moment effectively smears out the nuclear surface, accounting for the integration of the Y_{20} deformation over angles.

One could also modify the c parameter rather than the t parameter to match the Barrett moment. This results in a negligible difference in the overlap integrals.

¹ If the available literature does not provide a 2-parameter Fermi distribution - some electron scattering measurements use a Fourier-Bessel expansion -, we use a least square method to fit the distribution to a 2pF

² This is not to be confused with the spherical three-parameter Fermi distribution often used in electrons scattering from heavy nuclei.

3. Dataset

Our calculations employ a compilation of data from different sources, which we list in the footnotes to Table A of the Appendix (in which BM stands for Barrett Moment). When there are different sources for data on an isotope, we use the data from the compilation listing the largest number of isotopes.

- Nuclear charge distribution parameters:

The vast majority come from Fricke *et al.* [33] (Table III.A and III.C), a compilation of muonic X-ray and electron scattering experimental data. We add several muonic X-ray measurements [34–37] that were not included in Fricke *et al.*. When muonic X-ray measurements do not exist, we use the compilation of electron scattering experimental data from de Vries *et al.* [17]. When the only information available is the proton *rms* radius, we use data from Angeli *et al.* [38].

For quadrupole deformations we use the model of Möller *et al.* [39] for most isotopes. This employs a Finite-Range Drop Model (FRDM) to compute ground-state quadrupole deformations, as well as many other nuclear properties. When available, we also use the Zhang *et al.* [25] model that calculates separate quadrupole deformations for proton and neutron distributions.

- Neutron distribution:

We use the Zhang *et al.* [25] deformed relativistic Hartree-Bogoliubov model to separately evaluate the proton and the neutron nuclear distributions. This model only treats even-even nuclei, avoiding the additional single particle effects on both charge and neutron distributions seen in even-odd and odd-even nuclei.

4. Uncertainties

We consider two sources of systematic uncertainties: the quadrupole deformation β and the radius at half maximum c in the Fermi distribution.

We take the quadrupole deformation error from Stelson and Grodzins [22], where uncertainty on $B(E2)$ is converted into uncertainty on β assuming a uniform ellipsoidal charge distribution. The uncertainty on c is taken directly from Fricke *et al.* [33].

The relative uncertainty on c does not exceed 2%, while the relative uncertainty on β can be up to 20%. We therefore propagated only the uncertainty in β to the Barrett moment and ignored the c uncertainty.

The resulting relative uncertainty on the Barrett moment on all the available elements never exceeded 1%; we show the values for the Neodymium isotopes in Table I and Fig. 2 as an example.

C. Results

The resulting overlap integrals calculated on the 236 stable isotopes with natural abundance above 1% are displayed in Figure 4. The plot compares the results of Heeck *et al.* [12]; our new results are in general agreement. The main difference appears in the deformed nuclei region ($60 < Z < 80$), where our values are higher due to our explicit treatment of the effect of the deformation on the matrix elements. This results in a smoother decrease of the overlap integral value after $Z = 60$. This illustrates our attempts to deconvolute the New Physics interaction from the nuclear effects.

Figure 5 shows the overlap integrals weighted by natural abundance, in comparison with work from Kitano *et al.* [10]. The latter does not use natural abundance weighting but only displays one isotope per element. Again, the main difference between the two datasets is in the deformed nuclei region.

From the overlap integrals, we can compute the conversion rate using Eq. 2 for all the elements, and we obtain the sensitivity of different target materials normalized to the conversion rate in ^{27}Al . In Fig. 6 our result is compared to that from Cirigliano *et al.* [11]. Four physics models are considered: dipole (D), scalar (S) and two vector type ($V^{(\gamma)}$ and $V^{(Z)}$). $V^{(\gamma)}$ describes the scenarios where the transition charge radius operator gives the dominant contribution to the CLFV Lagrangian, and $V^{(Z)}$ describes the case where the dominant operator is assumed to be an effective Z -penguin [40]. Some candidate complementary target nuclei for future conversion measurements are highlighted, further discussion is presented in Sec. V.

Figure 7 removes the normalization relative to muon capture and shows the relative conversion rates in each material relative to that in ^{27}Al . The objective is to separate the coherent muon conversion from the incoherent muon capture our motivation for this presentation of our results is detailed in Sec. IV.

IV. NORMALIZATION AND (Z, A) DEPENDENCE OF THE CONVERSION RATE

The conventional approach to the normalization of $\mu \rightarrow e$ conversion experiments, quoting the conversion rate (experimental limit or theory prediction) normalized to the measured rate of μ capture on a given nucleus, has been in place for more than seventy years. We will discuss the shortcomings of this convention and propose a revised presentation of $\mu \rightarrow e$ conversion results that addresses our concerns.

The first limit on $\mu \rightarrow e$ conversion, by Lagarrigue and Peyrou [41], using cosmic ray muons stopped in copper and tin targets in a Wilson cloud chamber, employed previous measurements of the muon lifetime (dominated by muon capture in this regime) in copper and antimony [42] as normalization. The first accelerator experiment, using

a copper target [43], also normalized to the (directly measured) rate of muon capture.

The choice to normalize to the muon capture rate is not precisely analogous to the idea of a branching fraction (the number of decays into a particular mode, divided by all decays), which would be to divide the conversion rate in the field of a particular nucleus by all possible fates of the muon ($\mu \rightarrow e$ conversion, decay in orbit or nuclear capture). This normalization is essentially a historical convention initially codified by the work of Weinberg and Feinberg in 1959 [21]. All results or predictions on muon-to-electron conversion have henceforth been presented in the form $R_{\mu \rightarrow e}$ (Eq. 1).

Compilations of the history of experimental limits on CLFV processes typically present the 90% confidence level limits for decays and conversion on the same plot. This analogy ignores the fact that decay and conversion experiments are normalized differently. The decay limits are reported as true branching fractions, while the conversion rate limits are on the fraction of muon captures resulting in the production of a mono-energetic electron, which does not account for all fates of a muon in a muonic atom. Indeed, the lifetime of such a muon is determined in varying proportions by the conversion rate, a BSM process, by the nuclear capture rate, an incoherent Standard Model process, and by the lifetime of the decay-in-orbit muon, which is modified from the free decay rate by the atomic binding energy, the so-called Huff factor (0.993 for aluminum, 0.981 for titanium and 0.850 for gold) [44].

It is clear from these points that a revised approach is desirable. In particular, one would like to avoid the spurious introduction of nuclear effects into the presentation of a conversion result to the greatest extent possible in order to facilitate a conceptually cleaner comparison with results from decay experiments.

Normalizing an experimental conversion result requires determination of the number of stopped muons within the sensitive time window of the experiment. This involves muon decay as well as nuclear muon capture. In the upcoming Mu2e experiment downstream detectors count $2P - 1S$ muonic X-rays or other transitions and delayed γ -rays from muon capture to infer the stopped muon rate. This measured rate is then used to normalize the conversion rate limit or observation.

Table II lists the muon capture reactions in ^{27}Al , which produce states of Mg, Na, and Ne [45]. Note that only 13% of captures result in the ^{27}Mg ground state. The majority of captures result in neutron emission, with the nucleus left in either ground or excited states. The detailed calculation of the relevant nuclear matrix elements is quite complex, which is the reason the experimentally measured value of the total μ capture rate is used in deriving a conversion experiment's single event sensitivity. This is an important part of the normalization: the number of stopped muons in the sensitive time window of the experiment.

The experimental measurement of the total muon lifetime, with its associated uncertainties, thus unavoidably

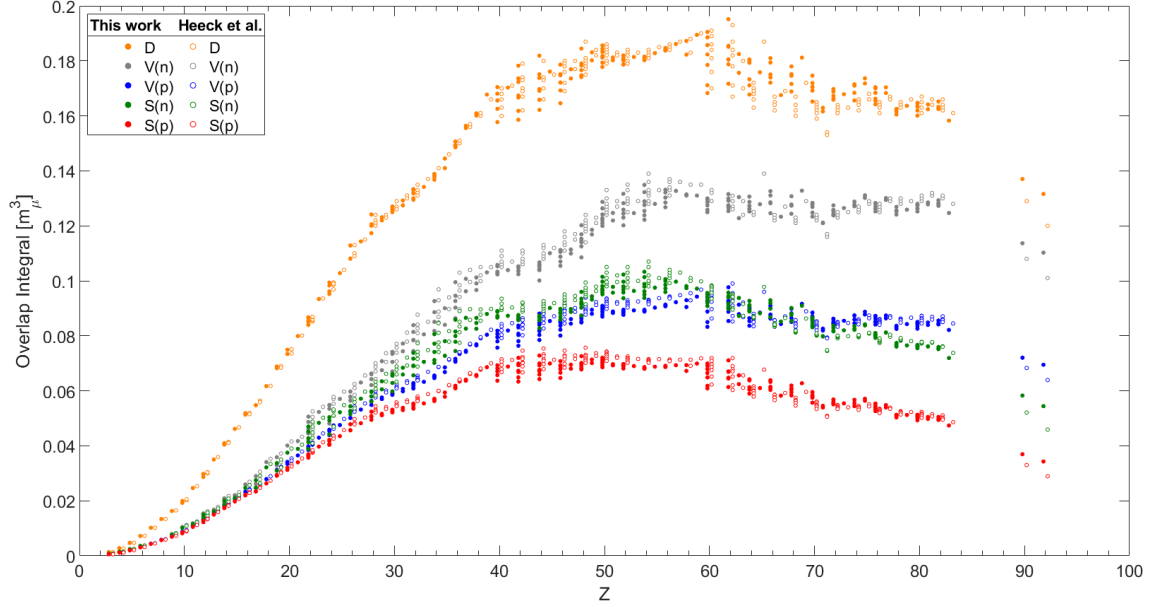


FIG. 4. The overlap integrals for dipole, vector and scalar couplings as a function of atomic number for isotopes having a natural abundance $> 90\%$, for the compilation of Heeck *et al.*[12] and this work. For clarity, we shift the result of Heeck *et al.* by $+\frac{1}{2}$ on the x-axis.

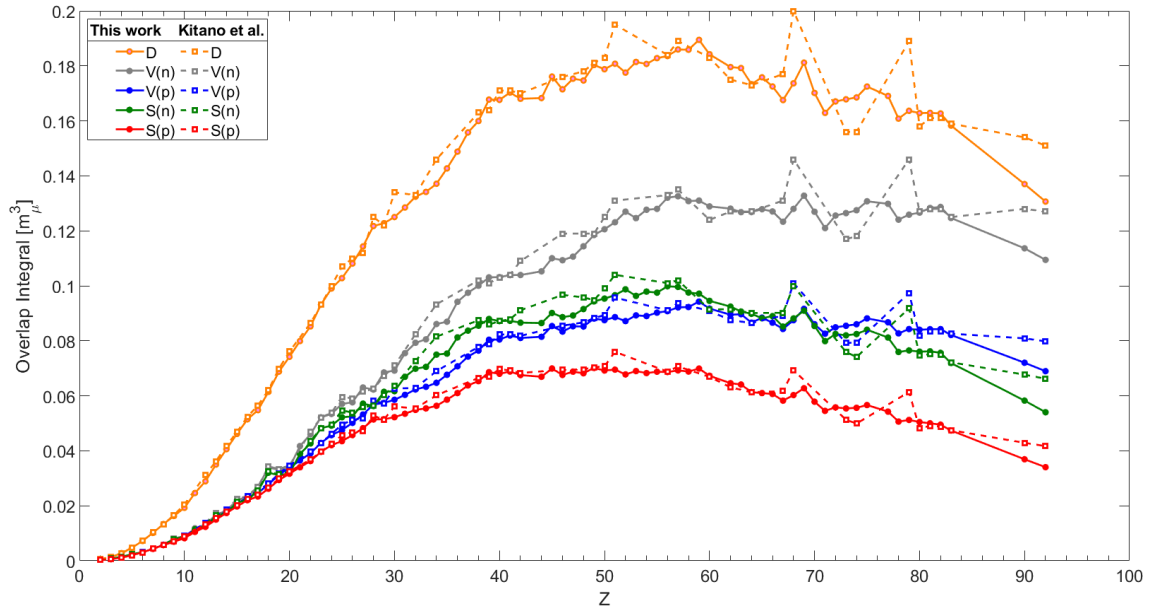


FIG. 5. The overlap integrals for dipole, vector and scalar couplings as a function of atomic number for each element, weighted by natural abundance, for the compilation of Kitano *et al.*[10, 11] and this work.

involves the calculation of the experimental efficiency and therefore the calculation of the $\mu \rightarrow e$ conversion rate. Since the overlap of the muon atomic wave function with the nuclear proton and neutron distribution

influences the effective lifetime, the New Physics and the Standard Model nuclear physics are inextricably mixed: the measured rate (or limit on the rate) manifestly depends on the muon capture lifetime. The muon nuclear

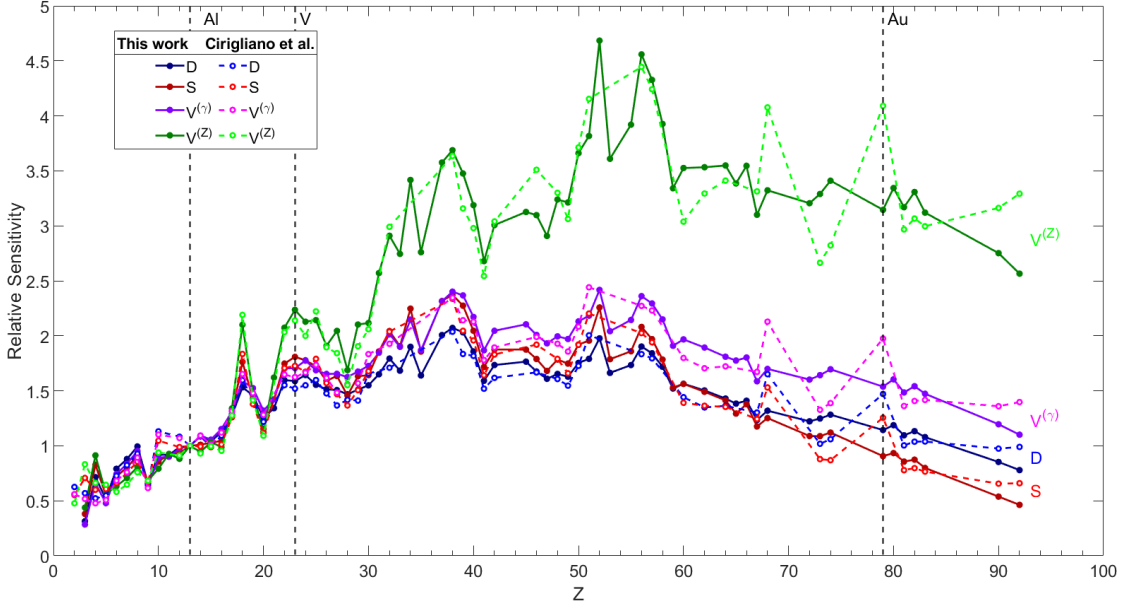


FIG. 6. Comparison with of our results on sensitivity as a function of Z with those of Cirigliano *et al.*[11]. The conversion rates are normalized to the muon capture rate and are relative to the rate for aluminum.

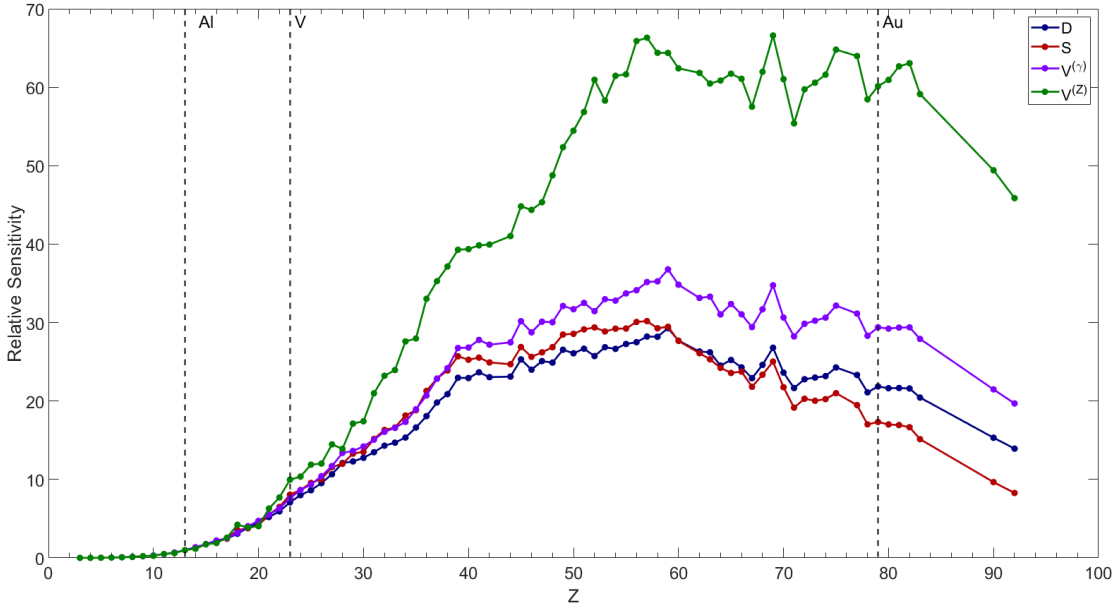


FIG. 7. Our calculation of the experimental sensitivity of CLFV experiments as a function of atomic number. The conversion rate is not normalized to the muon capture rate.

capture rate *grosso modo* follows Wheeler’s [46] Z_{eff}^4 law, but in detail shows the effect of nuclear shell structure on nuclear size. The convention of quoting a “capture fraction”, thereby exaggerates the effect of nuclear shell model structure.

An explicit example can be found in equation (3) in the report of the SINDRUM II limit on the conversion rate in lead (Pb) [47], where the denominator in the calculation of $B_{\mu e}$ is $f_{\text{capt}} N_{\text{stop}} \epsilon_{\text{tot}}$. Since f_{capt} for Pb is 0.95, the normalization to μ capture is only slightly dif-

TABLE I. Comparison of muonic X-ray and electron scattering determinations of three-parameter Fermi distributions in neodymium isotopes.

Isotope	c (fm)	t (fm)	β	rms radius (fm)	Barrett Moment
Muonic X-ray[30]					
^{142}Nd	5.80 ± 0.03	2.32 ± 0.08	0.104 ± 0.02	4.91 ± 0.08	15.99 ± 0.03
^{144}Nd	5.85 ± 0.03	2.27 ± 0.08	0.123 ± 0.02	4.94 ± 0.08	16.11 ± 0.04
^{146}Nd	5.82 ± 0.03	2.42 ± 0.08	0.151 ± 0.02	4.98 ± 0.08	16.26 ± 0.06
^{148}Nd	5.84 ± 0.03	2.40 ± 0.08	0.197 ± 0.04	5.00 ± 0.08	16.38 ± 0.13
^{150}Nd	5.86 ± 0.03	2.35 ± 0.08	0.279 ± 0.005	5.05 ± 0.08	16.58 ± 0.01
Electron Scattering [29]					
^{142}Nd	5.7045 ± 0.03	2.539 ± 0.013	0.104 ± 0.02	4.92 ± 0.08	15.98 ± 0.03
^{144}Nd	5.6634 ± 0.03	2.696 ± 0.013	0.123 ± 0.02	4.96 ± 0.08	16.11 ± 0.04
^{146}Nd	5.6600 ± 0.03	2.760 ± 0.013	0.151 ± 0.02	4.99 ± 0.08	16.23 ± 0.06
^{148}Nd	5.6871 ± 0.03	2.798 ± 0.022	0.197 ± 0.04	5.04 ± 0.08	16.46 ± 0.13
^{150}Nd	5.7185 ± 0.03	2.861 ± 0.031	0.279 ± 0.005	5.13 ± 0.08	16.86 ± 0.01

TABLE II. Muon capture rates on ^{27}Al leading to Mg, Na and Ne final states (from [45]).

Reaction	Observed γ -ray yield	Estimated ground-state transition	Missing yields	Total yield
$^{27}\text{Al}(\mu^-, \nu)^{27}\text{Mg}$	10(1)	0	3	13
$^{27}\text{Al}(\mu^-, \nu n)^{26}\text{Mg}$	53(5)	4	4	61
$^{27}\text{Al}(\mu^-, \nu 2n)^{25}\text{Mg}$	7(1)	3	2	12
$^{27}\text{Al}(\mu^-, \nu 3n)^{24}\text{Mg}$	2	3	1	6
$^{27}\text{Al}(\mu^-, \nu p \alpha n)^{26-23}\text{Na}$	2	2	1	5
$^{27}\text{Al}(\mu^-, \nu \alpha \alpha n)^{23-21}\text{Ne}$	1	2	0	3
Total	75(5)	14	11	100

ferent from the normalization to muon stops. For lighter nuclei, however, for example, aluminum, f_{capt} is 0.61, so the change in normalization amounts to 64%. Further, since the μ capture rate as a function of atomic number reflects nuclear shell structure as well the details of the low-lying levels of individual nuclei, and is primarily an incoherent process, its use introduces extraneous nuclear physics into consideration of the Z dependence of the coherent New Physics process of μ to e conversion.

From a theoretical perspective, a model calculation of the rate of conversion effectively yields an absolute rate (more specifically, a rate characterized by G_F^2 and a mass-scale coupling factor). The conventional normalization involves a hybrid ratio of the calculated rate of the coherent conversion process divided by the experimental measurement of a partially incoherent muon capture process. This has not mattered in any practical sense up to this point, but makes conceptual comparisons with decay experiments unnecessarily difficult. We should remove this inconsistency before we begin to compare conversion rates for different nuclei to explore the Lorentz structure of the conversion process.

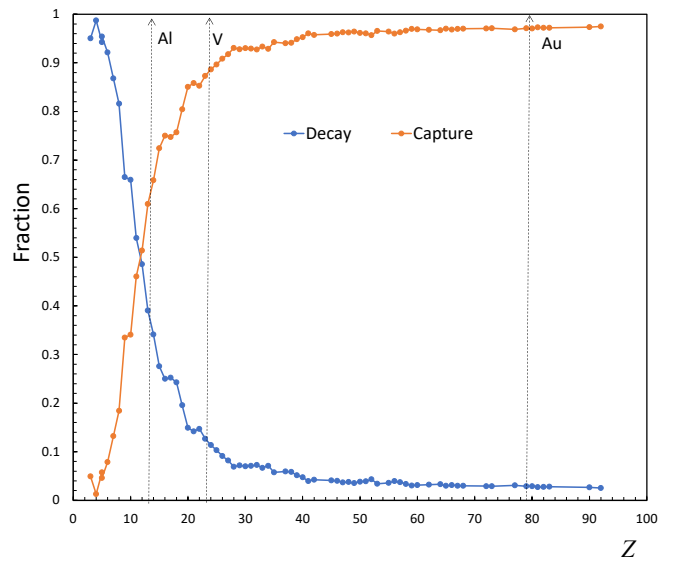


FIG. 8. The fraction of muon decay in orbit (DIO) in a muonic atom compared to the μ^- capture rate as a function of Z . Experimental values are taken from the Measday compilation [20], a survey experiment [44] or a specific previous experiment (Ref. [45] for ^{27}Al).

Crivellin *et al.* [58] write the conversion rate, not the conversion ratio, as

$$\Gamma_{\mu \rightarrow e}^N = \frac{m_\mu^5}{4\Lambda^4} |eC_L^D D_N + 4(G_F m_\mu m_p \tilde{C}_{(p)}^{SL} S_N^{(p)})| \quad (7)$$

$$+ |\tilde{C}_{(p)}^{VR} V_N^{(p)} + p \rightarrow n|^2 + L \leftrightarrow R, \quad (8)$$

involving the proton and neutron fields, but otherwise similar to the muon decay rates.

The historical normalization of this process to the muon capture rate conflates the actual sensitivity of a

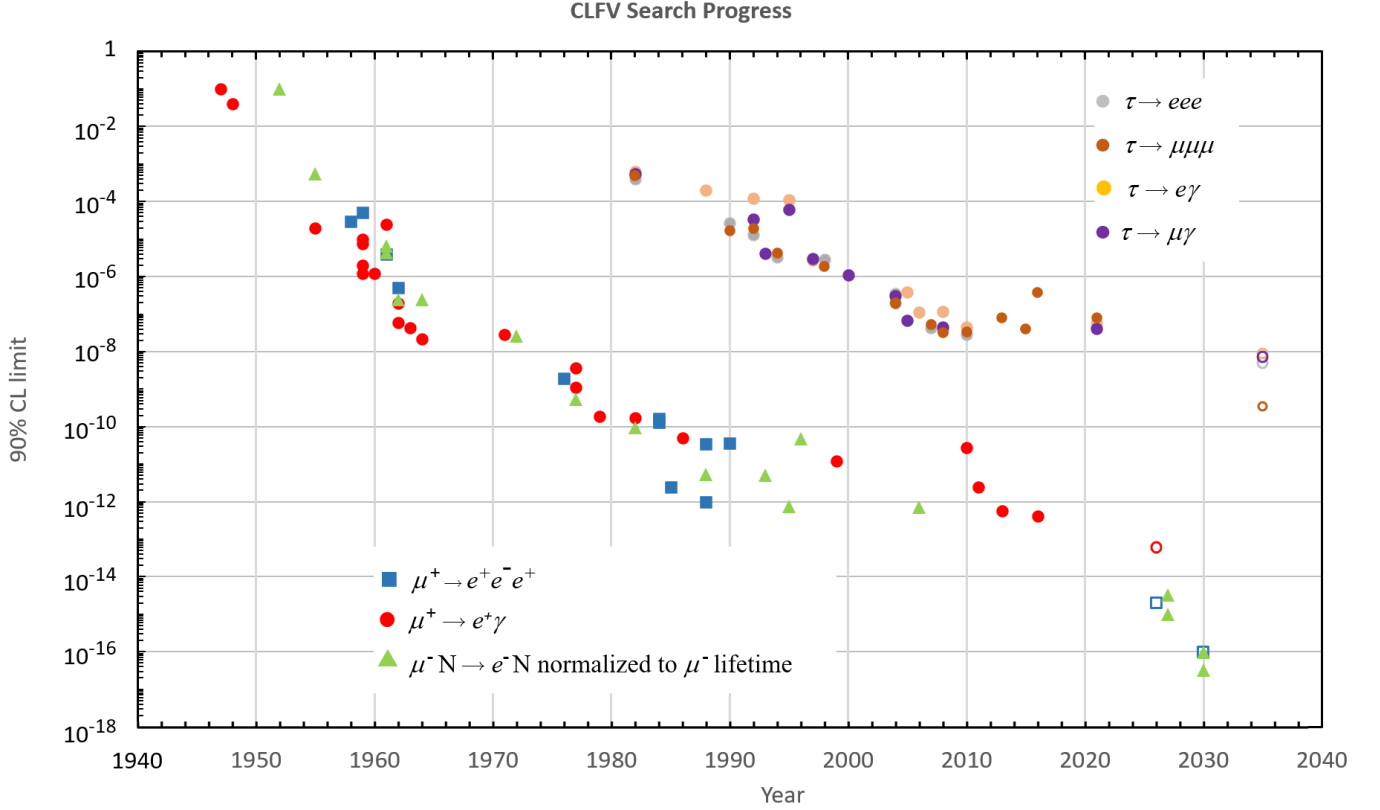


FIG. 9. Chronology of 90% confidence limits on $\mu \rightarrow e\gamma$, $\mu \rightarrow 3e$, μ to e conversion, $\tau \rightarrow e\gamma$, $\tau \rightarrow \mu\gamma$ and $\tau \rightarrow 3e$, including predicted limits for current experiments. The μ to e conversion results are normalized to the total muon lifetime, not the heretofore conventional μ capture rate. Unfilled symbols represent the goals of experiments currently in preparation. Further improvement in search sensitivity is possible with new stopped muon beams under study for decades hence.

TABLE III. Atomic number-dependent adjustment of $\mu \rightarrow e$ conversion limits to normalization to muon stops rather than captures.

Year	Reference	Nucleus	90% CL Limit Normalized to μ Capture	90% CL Limit Normalized to μ Stops
1952	[41]	Sn, Sb	1.0×10^{-1}	1.0×10^{-1}
1955	[43]	Cu	5.0×10^{-4}	5.4×10^{-4}
1961	[48]	Cu	4.0×10^{-6}	4.3×10^{-6}
1961	[49]	Cu	5.9×10^{-6}	6.4×10^{-6}
1962	[50]	Cu	2.2×10^{-7}	2.4×10^{-7}
1964	[51]	Cu	2.2×10^{-7}	2.4×10^{-7}
1972	[52]	Cu	2.6×10^{-8}	2.8×10^{-8}
1977	[53]	S	4.0×10^{-10}	5.3×10^{-10}
1982	[54]	S	7.0×10^{-11}	9.3×10^{-11}
1988	[55]	Ti	4.6×10^{-12}	5.4×10^{-12}
1993	[56]	Ti	4.3×10^{-12}	5.0×10^{-12}
1995	[57]	Ti	6.5×10^{-13}	7.6×10^{-13}
1996	[47]	Pb	4.6×10^{-11}	4.7×10^{-11}
2006	[1]	Au	7.0×10^{-13}	7.2×10^{-13}

conversion experiment with the nuclear physics of muon capture. In the background-free case the experimental

sensitivity depends only on the number of conversion electrons in the signal window over the sensitive time of the experiment, which is also true of a rare decay experiment. Why then should we insert an extraneous muon capture factor into the many theory comparisons of conversion *vs.* decay sensitivity against particular models?

The limits normalized to muon stops and muon capture are listed in Table III. Fig. 6 presents our calculation of the (Z, A) dependence of the CLFV matrix elements without the muon capture normalization, demonstrating the much-reduced extraneous structure heretofore introduced by normalization to the muon capture rate.

Fig. 9 shows the existing $\mu \rightarrow e$ conversion and decay experimental limits. Here we normalize the conversion results to muon stops, removing the historical muon capture normalization, making the comparison with decay experiments more intuitive.

V. SPIN-DEPENDENCE AND TARGET DESIGN CONSIDERATIONS

Coherent muon-to-electron conversion in a nucleus results in the emission of a mono-energetic electron with

an energy $E_{\mu e}$ that is nuclear dependent (104.97 MeV for aluminum (Al)). Radiative corrections to the conversion electron spectrum have been calculated by Szafron [59]. The time distribution of the conversion electron depends on the mean lifetime of the muonic atom and is also nucleus-dependent.

The dominant intrinsic background in a conversion search is electrons from decay-in-orbit (DIO). The momentum spectrum of these electrons differs from that of electrons from free muon decay, which follows the Michel spectrum with an endpoint of ~ 52 MeV/c. When the muon decay occurs in the nuclear field there is a recoil tail and there are significant radiative corrections [60, 61]. The resulting endpoint of the electron momentum spectrum is close to the conversion electron signal. Consequently, to detect the conversion electron an experiment must have detectors with a momentum resolution capable of distinguishing these recoil tail decay electrons from the conversion signal electrons. Energy straggling in the target material must be minimized to maintain good signal-to-background discrimination. Radiative pion capture (RPC) backgrounds are produced when pions in the muon beamline stop in the target. The pion is captured into the orbit of the nucleus, resulting in emission of a photon, $\pi^- + N(A, Z) \rightarrow \gamma^{(*)} + N(A, Z-1)$, followed by an asymmetric ($\gamma \rightarrow e^+e^-$) conversion producing electrons with energies nearly up to the charged pion mass (139 MeV/c²). The upcoming experiments Mu2e and COMET mitigate pion backgrounds through the use of pulsed beams and by exploiting the short pion lifetime (~ 26 ns at rest) and ignore particles in their detectors arriving before a few hundred ns. Cosmic ray-induced backgrounds also contribute significantly if not vetoed, but have a small dependence on stopping target design [62].

We consider the phenomenological advantages of four proposed elements: titanium, vanadium, lithium, and gold. Table IV provides details of these materials including their densities, mean muonic atom lifetimes, isotope abundance, and the nuclear spins of these isotopes. All these features have an impact on the New Physics we could observe in these targets. The experimental values for capture and decay fractions are taken from the Measday compilation [20], a survey experiment [44] or a specific previous experiment (Ref. [45] for ²⁷Al). Figure 8 shows the variation of the average capture and decay fractions with atomic number. Heavier nuclei have smaller decay fractions and larger capture fractions, which is beneficial, as it results in fewer decay background electrons for the same number of stopped muons.

In reality, the conversion target choice is a compromise between maximizing the number of stopped muons while minimizing the scattering and energy losses experienced by the outgoing electrons. For example, the Mu2e experiment plans to utilize a foil-based target consisting of 37 thin (~ 100 μm thick) foils orientated along the beam axis, based on detailed simulations [63].

TABLE IV. Elements and their characteristics (atomic number (Z), density (ρ), lifetime (τ_{mean}), and relative average fraction of decay ($f_{dec.}$) to capture ($f_{capt.}$) along with their naturally occurring abundance ($Ab.$) for given isotopes ($I.$), and their nuclear spins (s). Lifetimes taken from Ref. [44].

Element	Z	ρ [g/cm ³]	τ_{mean} [ns]	$f_{dec.}$ [%]	$f_{capt.}$ [%]	$I.$	$Ab.$ [%]	s
Li	3	0.534	2175	99	1	⁶ Li	7.6	1
						⁷ Li	92.4	3/2
Al	13	2.11	864	39	61	²⁷ Al	100	5/2
Ti	22	4.51	329	15	85	⁴⁶ Ti	8.25	0
						⁴⁷ Ti	7.44	5/2
						⁴⁸ Ti	73.72	0
						⁴⁹ Ti	5.41	7/2
						⁵⁰ Ti	5.18	0
V	23	6.11	284	13	87	⁵⁰ V	0.25	6
						⁵¹ V	99.75	7/2
Au	79	19.3	73	3	97	¹⁹⁷ Au	100	3/2

A. Practical Considerations

From Figs. 6 and 7 it is apparent that both titanium (Ti) and vanadium (V) have the advantage that, if coherent conversion is measured in Al, they provide good separation in the relative conversion rates produced by the dipole, scalar, and vector interactions. This makes them useful for determining the type of physics responsible for a coherent conversion. From a practical point-of-view, Ti and V can be readily obtained in solid, foil form. In addition, Table IV shows that the mean lifetime of a muonic Ti or V atom is much shorter than for Al, but is not so short that pion-induced background would overwhelm the conversion signal. Both Ti and V have smaller average decay fractions than Al, meaning lower decay backgrounds for the same number of stopped muons. For all these reasons Ti and V are popular choices for the next generation of conversion measurements, assuming a signal in Mu2e or COMET.

Lithium (Li) is another potential alternative target material. The muonic lifetime in Li is close to the free muon lifetime; as a result, the survival fraction is just a few percent. The relative proportion of decays would be much larger than in Al, meaning more decay background for the same number of stopped muons. Due to the much smaller survival fraction, reaching the same sensitivity as aluminum would require much longer running time. From a practical point of view, a Li foil target is feasible. Lithium has been used in foil form in a transition radiation detector [64]. Since Li has a much lower density, ~ 4 times less than Al, stopping the same number of muons would require a much larger target volume.

From Figs. 6 and 7 it is also clear that the conversion rates, relative to Al, for dipole, scalar, and vector interactions show largest differences for high Z nuclei, making gold (Au) an obvious choice for establishing the nature of

the physics, assuming a signal in Al. Table IV shows that the relative fraction of decay to capture in Au is small, meaning on average 3 % of muons will undergo decay, a significant reduction from 39 % in Al. The downside comes from the fact that Au has a mean muonic atom lifetime of just 73 ns. It would not be feasible to use a Au target in a Mu2e or COMET style design due to the enforced time selection required to remove pion-induced backgrounds and the beam structure at these current facilities. If pion contamination could be eliminated using a Fixed Field Alternating-gradient machine such as in the proposed Advanced Muon Facility [14], measuring conversion in Au could be feasible.

B. Considering Incoherent Contributions

The mono-energetic electron experimental signature of $\mu \rightarrow e$ conversion selects the spin-independent (SI) coherent interaction with the charge or mass distribution, which is proportional to A^2 . Spin-dependent (SD) contributions do not have coherent enhancement and have been studied in Refs. [16, 65]. Thus far we have considered only coherent contributions from a dipole, scalar, and vector interaction these operators will contribute to the SI rate, while axial, tensor, and pseudoscalar operators contribute to the SD rate. The SD rate depends on the distribution of spin in the nucleus [66], and therefore requires detailed modeling of the target nucleus. In most models, SI conversion dominates due to the A^2 enhancement, but this is not true in all New Physics models. Reference [67] describes how the SD interaction induced by $\text{ALP}-\pi^0$ mixing is the leading contribution to $\mu \rightarrow e$ conversion in models where axion-like particles (ALPs) induce the conversion. Consequently, in the event a conversion signal is observed, it is important to consider of the spin of the target nuclei to understand the Lorentz structure of the New Physics.

Natural titanium has several stable isotopes with different spins, however, separated isotopes of Ti are not readily available in the quantities needed for a target of ~ 200 g. Employing a natural Ti target complicates the unraveling of SD and SI conversion rates. Vanadium is therefore an attractive alternative to Ti; it provides the same physics benefits (increased survival fraction, similar muonic lifetime, *etc.*) with the advantage that it has a single stable isotope, ^{51}V (spin $\frac{7}{2}$), with $> 99\%$ abundance. Vanadium is also readily available in thin foils that can be fabricated into a target similar to the Al target used in Mu2e.

Comparing conversion in light targets with very different neutron-to-proton ratios (for example lithium (Li) and Al) could allow us to distinguish operators involving neutrons from those involving protons [65]. Additionally, Ref. [16] suggests that a conversion measurement in lighter nuclei, such as Li, would be of interest for detecting SD conversion, since the SD rate being relatively suppressed by $1/A^2$ compared to the SI rate. As a result,

the ratio Γ_{SD}/Γ_{SI} is larger in lighter nuclei. For these reasons Au (which, in addition, has only a single stable isotope) is also an attractive option.

When choosing the target material for the next generation of conversion experiments it is important to consider more than the conversion rate relative to Al. We must also take into account the relative decay fraction, muonic atom lifetime, and availability of isotopes of a known spin; we have described four possible target choices All have physics advantages; the specific target chosen will depend on, and influence, the experimental design of any future facility, which is beyond the scope of this paper.

VI. CONCLUSIONS

To conclude, we have presented a new calculation of the (Z, A) dependence of coherent muon-to-electron conversion in 236 isotopes, significantly extending the previous studies of Kitano *et al.* [10] and Cirigliano *et al.* [11]. Our approach has several key improvements over these previous treatments:

- We have included the effect of permanent quadrupole deformation on the CLFV matrix elements, using the method of Barrett moments to add the substantial catalog of muonic X-ray nuclear size and shape determinations of the charge distribution to the electron scattering results used in previous calculations.
- Rather than using neutron distributions scaled by N/Z from charge distributions, as in the previous work, we have employed a Hartree-Bogoliubov model for even-even nuclei to calculate neutron-related matrix elements. This takes into account the quadrupole deformation of the neutron distributions as well as the fact that neutrons are in general in different shell model orbits than protons.
- We present the resulting CLFV overlap integrals for stable isotopes with greater than 1% abundance as well as results weighted for natural abundance.
- The resulting conversion rates differ from previous calculations, particularly in the region of large permanent quadrupole deformation.

Finally, we propose a revised normalization for $\mu \rightarrow e$ conversion results, quoting the measured conversion rate (or limit thereon) directly, instead of presenting the conversion rate divided by the muon capture rate, which is generally not measured in the same experiment.

Our sensitivity plots are presented in this form. Note the reduction in the scatter of points, which is largely due to the removal of the additional shell model structure observed in the incoherent muon capture process.

ACKNOWLEDGEMENTS

This work was supported in part by DOE Grant DE-SC0011925. It was initiated at the Aspen Center for Physics, which is supported by National Science Foundation grant PHY-2210452.

We wish to acknowledge helpful conversations with Wick Haxton, Julian Heeck, Natalia Oreshkina, Robert Szafron and Petr Vogel, as well as the careful reading of the text by Bertrand Echenard, James Miller, Ryan Plestid and Frank Porter.

APPENDIX

A. Table of Overlap Integrals

Isotope	Z	N	BM	D	S(p)	V(p)	S(n)	V(n)
⁶ Li ^{a,b}	3	3	6.19	0.0013	0.00055	0.00055	0.00055	0.00055
⁷ Li ^{a,b}	3	4	5.36	0.0014	0.00058	0.00058	0.00077	0.00078
⁹ Be ^a	4	5	5.42	0.0028	0.00117	0.00118	0.00146	0.00147
¹⁰ B ^a	5	5	5.68	0.0047	0.00198	0.00200	0.00198	0.00200
¹¹ B ^{a,b}	5	6	5.46	0.0047	0.00201	0.00203	0.00241	0.00244
¹² C ^a	6	6	5.83	0.0072	0.00306	0.00310	0.00306	0.00310
¹³ C ^a	6	7	5.82	0.0072	0.00306	0.0031	0.00306	0.0031
¹⁴ N ^a	7	7	5.87	0.0102	0.00434	0.00441	0.00434	0.00441
¹⁶ O	8	8	6.76	0.0134	0.00571	0.00582	0.00571	0.00582
¹⁹ F	9	10	7.90	0.0163	0.00694	0.00711	0.00771	0.00790
²⁰ Ne	10	10	8.57	0.0193	0.00819	0.00842	0.00821	0.00844
²² Ne	10	12	8.31	0.0199	0.00850	0.00874	0.01015	0.0104
²³ Na	11	12	8.50	0.0246	0.0105	0.0108	0.0115	0.0118
²⁴ Mg	12	12	8.84	0.0287	0.0122	0.0127	0.0122	0.0127
²⁵ Mg	12	13	8.59	0.0297	0.0127	0.0131	0.0138	0.0142
²⁶ Mg	12	14	8.59	0.0298	0.0127	0.0131	0.0149	0.0154
²⁷ Al	13	14	8.76	0.0350	0.0150	0.0155	0.0161	0.0167
²⁸ Si	14	14	8.99	0.0406	0.0174	0.0181	0.0174	0.0181
²⁹ Si	14	15	8.94	0.0405	0.0173	0.0180	0.0186	0.0193
³⁰ Si	14	16	8.88	0.0410	0.0176	0.0183	0.0201	0.0209
³¹ P	15	16	9.11	0.0462	0.0198	0.0207	0.0211	0.0220
³² S	16	16	9.49	0.0519	0.0222	0.0233	0.0222	0.0233
³⁴ S	16	18	9.62	0.0513	0.0220	0.0231	0.0247	0.0259
³⁵ Cl ^c	17	18	10.31	0.0548	0.0234	0.0247	0.0248	0.0261
³⁷ Cl ^c	17	20	10.31	0.0547	0.0234	0.0246	0.0275	0.0290
⁴⁰ Ar	18	22	10.10	0.0617	0.0263	0.0279	0.0322	0.0341
³⁹ K	19	20	10.10	0.0688	0.0294	0.0313	0.0309	0.0329
⁴¹ K	19	22	10.20	0.0682	0.0291	0.0310	0.0337	0.0359
⁴⁰ Ca	20	20	10.30	0.0750	0.0320	0.0341	0.0320	0.0341
⁴⁴ Ca	20	24	10.52	0.0734	0.0313	0.0334	0.0375	0.0401
⁴⁵ Sc	21	24	10.63	0.0799	0.0340	0.0365	0.0389	0.0417
⁴⁶ Ti	22	24	10.92	0.0840	0.0357	0.0385	0.0388	0.0419
⁴⁷ Ti	22	25	10.87	0.0855	0.0364	0.0392	0.0413	0.0445
⁴⁸ Ti	22	26	10.84	0.0852	0.0362	0.0391	0.0428	0.0461
⁴⁹ Ti	22	27	10.75	0.0865	0.0368	0.0397	0.0452	0.0487
⁵⁰ Ti	22	28	10.72	0.0868	0.0369	0.0398	0.0470	0.0506
⁵¹ V	23	28	10.82	0.0934	0.0397	0.0430	0.0484	0.0523
⁵⁰ Cr	24	26	11.20	0.0962	0.0407	0.0443	0.0442	0.0481
⁵² Cr	24	28	10.96	0.0994	0.0422	0.0459	0.0492	0.0535
⁵³ Cr	24	29	11.06	0.0983	0.0417	0.0454	0.0504	0.0548
⁵⁴ Cr	24	30	11.30	0.0952	0.0403	0.0439	0.0504	0.0548
⁵⁵ Mn	25	30	11.38	0.103	0.0435	0.0475	0.0522	0.0571
⁵⁴ Fe	26	28	11.14	0.113	0.0478	0.0524	0.0515	0.0564
⁵⁶ Fe	26	30	11.43	0.108	0.0457	0.0502	0.0527	0.0579
⁵⁷ Fe	26	31	11.56	0.108	0.0456	0.0501	0.0544	0.0597

Isotope	Z	N	BM	D	S(p)	V(p)	S(n)	V(n)
⁵⁹ Co	27	32	11.70	0.114	0.0482	0.0532	0.0572	0.0630
⁵⁸ Ni	28	30	11.44	0.124	0.0524	0.0580	0.0562	0.0621
⁶⁰ Ni	28	32	11.64	0.121	0.0508	0.0563	0.0580	0.0642
⁶¹ Ni	28	33	11.74	0.120	0.0506	0.0560	0.0596	0.0660
⁶² Ni	28	34	11.84	0.117	0.0494	0.0549	0.0598	0.0663
⁶³ Cu	29	34	12.05	0.123	0.0517	0.0576	0.0606	0.0675
⁶⁵ Cu	29	36	12.13	0.122	0.0511	0.0570	0.0635	0.0708
⁶⁴ Zn	30	34	12.29	0.126	0.0527	0.0591	0.0598	0.0670
⁶⁶ Zn	30	36	12.38	0.125	0.0524	0.0588	0.0629	0.0705
⁶⁷ Zn ^d	30	37	12.28	0.127	0.0531	0.0595	0.0655	0.0734
⁶⁸ Zn	30	38	12.43	0.125	0.0522	0.0585	0.0661	0.0742
⁶⁹ Ga	31	38	12.59	0.129	0.0538	0.0607	0.0659	0.0744
⁷¹ Ga	31	40	12.72	0.127	0.0530	0.0598	0.0684	0.0772
⁷⁰ Ge	32	38	12.87	0.133	0.0552	0.0626	0.0656	0.0745
⁷² Ge	32	40	12.96	0.133	0.0553	0.0628	0.0692	0.0785
⁷³ Ge	32	41	13.02	0.130	0.0538	0.0612	0.0690	0.0784
⁷⁴ Ge	32	42	13.09	0.132	0.0546	0.0620	0.0717	0.0814
⁷⁶ Ge	32	44	13.02	0.130	0.0535	0.0608	0.0738	0.0839
⁷⁵ As	33	42	13.16	0.134	0.0554	0.0633	0.0705	0.0805
⁷⁶ Se	34	42	13.36	0.138	0.0566	0.0651	0.0701	0.0806
⁷⁷ Se	34	43	13.38	0.137	0.0563	0.0647	0.0712	0.0818
⁷⁸ Se	34	44	13.25	0.139	0.0571	0.0656	0.0741	0.0851
⁸⁰ Se	34	46	13.25	0.138	0.0569	0.0653	0.0772	0.0886
⁸² Se	34	48	13.22	0.139	0.0569	0.0654	0.0807	0.0926
⁷⁹ Br	35	44	13.47	0.141	0.0579	0.0668	0.0728	0.0840
⁸¹ Br	35	46	13.23	0.144	0.0594	0.0685	0.0781	0.0901
⁸⁰ Kr	36	44	13.63	0.149	0.0609	0.0706	0.0745	0.0864
⁸² Kr	36	46	13.39	0.149	0.0609	0.0706	0.0778	0.0903
⁸³ Kr	36	47	13.35	0.149	0.0612	0.0710	0.0799	0.0927
⁸⁴ Kr	36	48	13.32	0.149	0.0611	0.0709	0.0816	0.0946
⁸⁶ Kr	36	50	13.27	0.151	0.0618	0.0717	0.0859	0.0995
⁸⁵ Rb	37	48	13.31	0.156	0.0637	0.0742	0.0826	0.0962
⁸⁷ Rb	37	50	13.27	0.156	0.0641	0.0746	0.0866	0.1008
⁸⁶ Sr	38	48	13.43	0.160	0.0654	0.0765	0.0826	0.0967
⁸⁷ Sr	38	49	13.41	0.161	0.0657	0.0768	0.0847	0.0991
⁸⁸ Sr	38	50	13.40	0.161	0.0657	0.0769	0.0865	0.101
⁸⁹ Y ^c	39	50	13.43	0.168	0.0686	0.0804	0.0879	0.103
⁹⁰ Zr	40	50	13.53	0.170	0.0693	0.0819	0.0866	0.102
⁹¹ Zr	40	51	13.64	0.168	0.0682	0.0807	0.0870	0.103
⁹² Zr	40	52	13.74	0.166	0.0671	0.0795	0.0872	0.103
⁹⁴ Zr	40	54	13.98	0.163	0.0657	0.0780	0.0887	0.105
⁹⁶ Zr	40	56	14.25	0.158	0.0637	0.0757	0.0890	0.106
⁹³ Nb	41	52	13.75	0.170	0.0688	0.0819	0.0873	0.104
⁹² Mo	42	50	13.69	0.178	0.0720	0.0860	0.0857	0.102
⁹⁴ Mo	42	52	13.88	0.174	0.0699	0.0837	0.0866	0.104
⁹⁵ Mo	42	53	13.93	0.172	0.0693	0.0831	0.0875	0.105
⁹⁶ Mo	42	54	14.15	0.167	0.0673	0.0808	0.0863	0.104
⁹⁷ Mo	42	55	14.20	0.167	0.0669	0.0803	0.0876	0.105
⁹⁸ Mo	42	56	14.37	0.162	0.0649	0.0781	0.0862	0.104

Isotope	Z	N	BM	D	S(p)	V(p)	S(n)	V(n)	Isotope	Z	N	BM	D	S(p)	V(p)	S(n)	V(n)
¹⁰⁰ Mo	42	58	14.66	0.159	0.0634	0.0764	0.0873	0.105	¹³³ Cs	55	78	15.65	0.183	0.0688	0.0903	0.0975	0.128
⁹⁶ Ru	44	50	14.07	0.182	0.0728	0.0881	0.0828	0.100	¹³⁴ Ba	56	78	15.75	0.184	0.0687	0.0907	0.0959	0.127
⁹⁸ Ru	44	54	14.32	0.175	0.0700	0.0849	0.0857	0.104	¹³⁵ Ba	56	79	15.74	0.184	0.0689	0.0911	0.0972	0.128
⁹⁹ Ru	44	55	14.41	0.174	0.0693	0.0841	0.0866	0.105	¹³⁶ Ba	56	80	15.70	0.184	0.0689	0.0911	0.0986	0.130
¹⁰⁰ Ru	44	56	14.55	0.170	0.0676	0.0822	0.0857	0.104	¹³⁷ Ba	56	81	15.70	0.185	0.0691	0.0913	0.100	0.132
¹⁰¹ Ru	44	57	14.61	0.169	0.0672	0.0818	0.0871	0.106	¹³⁸ Ba	56	82	15.72	0.184	0.0687	0.0909	0.101	0.133
¹⁰² Ru	44	58	14.74	0.166	0.0659	0.0803	0.0866	0.105	¹³⁹ La	57	82	15.77	0.186	0.0693	0.0922	0.100	0.133
¹⁰⁴ Ru	44	60	15.02	0.162	0.0643	0.0785	0.0874	0.107	¹⁴⁰ Ce	58	82	15.85	0.187	0.0694	0.0930	0.0981	0.131
¹⁰³ Rh ^d	45	58	14.49	0.176	0.0699	0.0854	0.0901	0.110	¹⁴² Ce	58	84	16.00	0.182	0.0672	0.0905	0.0974	0.131
¹⁰² Pd	46	56	14.79	0.179	0.0708	0.0870	0.0859	0.105	¹⁴¹ Pr	59	82	15.92	0.189	0.0699	0.0943	0.0972	0.131
¹⁰⁴ Pd	46	58	14.94	0.175	0.0693	0.0852	0.0870	0.107	¹⁴² Nd	60	82	15.99	0.191	0.0699	0.0950	0.0956	0.130
¹⁰⁵ Pd	46	59	14.98	0.175	0.0689	0.0849	0.0884	0.109	¹⁴³ Nd	60	83	16.05	0.189	0.0691	0.0940	0.0956	0.130
¹⁰⁶ Pd	46	60	15.09	0.172	0.0679	0.0837	0.0882	0.109	¹⁴⁴ Nd	60	84	16.13	0.186	0.0679	0.0925	0.0950	0.130
¹⁰⁸ Pd	46	62	15.29	0.169	0.0666	0.0822	0.0895	0.111	¹⁴⁵ Nd	60	85	16.25	0.182	0.0665	0.0908	0.0942	0.129
¹¹⁰ Pd	46	64	15.46	0.165	0.0647	0.0801	0.0898	0.111	¹⁴⁶ Nd	60	86	16.38	0.179	0.0649	0.0888	0.0931	0.127
¹⁰⁷ Ag	47	60	14.88	0.177	0.0695	0.0861	0.0887	0.110	¹⁴⁸ Nd	60	88	16.60	0.171	0.0618	0.0850	0.0909	0.125
¹⁰⁹ Ag	47	62	15.01	0.174	0.0680	0.0844	0.0897	0.111	¹⁵⁰ Nd	60	90	16.47	0.168	0.0609	0.0833	0.0920	0.126
¹⁰⁶ Cd	48	58	14.69	0.184	0.0726	0.0902	0.0873	0.109	¹⁴⁴ Sm	62	82	16.06	0.195	0.0711	0.0977	0.0940	0.129
¹¹⁰ Cd	48	62	14.90	0.179	0.0701	0.0874	0.0903	0.113	¹⁴⁷ Sm	62	85	16.31	0.185	0.0669	0.0927	0.0917	0.127
¹¹¹ Cd	48	63	14.94	0.178	0.0697	0.0869	0.0914	0.114	¹⁴⁸ Sm	62	86	16.43	0.181	0.0646	0.0902	0.0898	0.125
¹¹² Cd	48	64	15.04	0.177	0.0690	0.0862	0.0918	0.115	¹⁴⁹ Sm	62	87	16.46	0.180	0.0648	0.0902	0.0909	0.127
¹¹³ Cd	48	65	15.08	0.175	0.0681	0.0851	0.0922	0.115	¹⁵⁰ Sm	62	88	16.45	0.185	0.0671	0.0922	0.0957	0.132
¹¹⁴ Cd	48	66	15.17	0.175	0.0681	0.0851	0.0935	0.117	¹⁵² Sm	62	90	16.55	0.179	0.0645	0.0888	0.0944	0.130
¹¹⁶ Cd	48	68	15.31	0.174	0.0678	0.0849	0.0960	0.120	¹⁵⁴ Sm	62	92	16.64	0.172	0.0614	0.0854	0.0917	0.127
¹¹³ In	49	64	14.93	0.183	0.0714	0.0895	0.0932	0.117	¹⁵¹ Eu	63	88	16.71	0.176	0.0625	0.0879	0.0872	0.123
¹¹⁵ In	49	66	15.04	0.180	0.0701	0.0880	0.0944	0.119	¹⁵³ Eu	63	90	16.61	0.182	0.0656	0.0913	0.0938	0.130
¹¹⁶ Sn	50	66	14.95	0.186	0.0720	0.0909	0.0951	0.120	¹⁵⁴ Gd	64	90	16.64	0.180	0.0641	0.0898	0.0908	0.127
¹¹⁷ Sn	50	67	15.00	0.184	0.0715	0.0903	0.0958	0.121	¹⁵⁵ Gd	64	91	16.65	0.180	0.0642	0.0905	0.0912	0.129
¹¹⁸ Sn	50	68	15.07	0.183	0.0710	0.0897	0.0966	0.122	¹⁵⁶ Gd	64	92	16.74	0.173	0.0613	0.0864	0.0888	0.125
¹¹⁹ Sn	50	69	15.10	0.182	0.0704	0.0890	0.0971	0.123	¹⁵⁷ Gd	64	93	16.72	0.179	0.0638	0.0899	0.0927	0.131
¹²⁰ Sn	50	70	15.13	0.181	0.0701	0.0887	0.0981	0.124	¹⁵⁸ Gd	64	94	16.84	0.171	0.0604	0.0853	0.0894	0.126
¹²² Sn	50	72	15.16	0.179	0.0693	0.0878	0.100	0.126	¹⁶⁰ Gd	64	96	16.89	0.168	0.0590	0.0837	0.0890	0.126
¹²⁴ Sn	50	74	15.22	0.178	0.0686	0.0870	0.101	0.129	¹⁵⁹ Tb ^e	65	94	16.62	0.176	0.0610	0.0884	0.0882	0.128
¹²¹ Sb	51	70	15.28	0.181	0.0697	0.0888	0.0957	0.122	¹⁶⁰ Dy ^d	66	94	17.06	0.174	0.0609	0.0875	0.0868	0.125
¹²³ Sb	51	72	15.31	0.180	0.0693	0.0883	0.0978	0.125	¹⁶¹ Dy	66	95	16.87	0.181	0.0639	0.0910	0.0919	0.131
¹²² Te	52	70	15.37	0.182	0.0698	0.0895	0.0937	0.120	¹⁶² Dy	66	96	16.91	0.175	0.0615	0.0877	0.0899	0.128
¹²⁴ Te	52	72	15.37	0.181	0.0693	0.0889	0.0958	0.123	¹⁶³ Dy	66	97	16.92	0.179	0.0632	0.0902	0.0929	0.133
¹²⁵ Te	52	73	15.38	0.181	0.0690	0.0887	0.0969	0.124	¹⁶⁴ Dy	66	98	17.01	0.172	0.0603	0.0863	0.0899	0.129
¹²⁶ Te	52	74	15.39	0.180	0.0689	0.0885	0.0980	0.126	¹⁶⁵ Ho ^f	67	98	17.42	0.168	0.0582	0.0843	0.0852	0.123
¹²⁸ Te	52	76	15.42	0.179	0.0681	0.0876	0.100	0.128	¹⁶⁴ Er ^d	68	96	17.28	0.175	0.0605	0.0881	0.0854	0.124
¹³⁰ Te	52	78	15.41	0.179	0.0682	0.0878	0.102	0.132	¹⁶⁶ Er	68	98	17.14	0.175	0.0609	0.0882	0.0880	0.127
¹²⁷ I	53	74	15.52	0.181	0.0690	0.0893	0.0963	0.125	¹⁶⁷ Er	68	99	17.21	0.178	0.0619	0.0898	0.0901	0.131
¹²⁸ Xe	54	74	15.70	0.181	0.0684	0.0891	0.0938	0.122	¹⁶⁸ Er	68	100	17.25	0.172	0.0595	0.0865	0.0876	0.127
¹²⁹ Xe	54	75	15.68	0.181	0.0684	0.0892	0.0950	0.124	¹⁷⁰ Er	68	102	17.34	0.169	0.0583	0.0850	0.0876	0.128
¹³⁰ Xe	54	76	15.66	0.181	0.0682	0.0889	0.0962	0.125	¹⁶⁹ Tm ^f	69	100	17.15	0.181	0.0628	0.0916	0.0910	0.133
¹³¹ Xe	54	77	15.65	0.182	0.0686	0.0895	0.0979	0.128	¹⁷⁰ Yb	70	100	17.29	0.170	0.0580	0.0861	0.0831	0.123
¹³² Xe	54	78	15.68	0.181	0.0683	0.0891	0.0989	0.129	¹⁷¹ Yb	70	101	17.33	0.175	0.0596	0.0885	0.0860	0.128
¹³⁴ Xe	54	80	15.63	0.181	0.0684	0.0892	0.101	0.132	¹⁷² Yb	70	102	17.38	0.169	0.0575	0.0855	0.0839	0.125
¹³⁶ Xe	54	82	15.67	0.180	0.0680	0.0888	0.103	0.135	¹⁷³ Yb	70	103	17.41	0.172	0.0585	0.0871	0.0860	0.128

Isotope	Z	N	BM	D	S(p)	V(p)	S(n)	V(n)	Isotope	Z	N	BM	D	S(p)	V(p)	S(n)	V(n)
¹⁷⁴ Yb	70	104	17.40	0.171	0.0581	0.0862	0.0866	0.128	¹⁹¹ Ir ^d	77	114	17.65	0.170	0.0548	0.0874	0.0812	0.129
¹⁷⁶ Yb	70	106	17.50	0.165	0.0557	0.0834	0.0847	0.127	¹⁹³ Ir ^d	77	116	17.68	0.168	0.0539	0.0864	0.0812	0.130
¹⁷⁵ Lu ^d	71	104	17.75	0.163	0.0545	0.0826	0.0799	0.121	¹⁹⁴ Pt	78	116	17.81	0.163	0.0513	0.0836	0.0761	0.124
¹⁷⁶ Lu ^d	71	105	17.77	0.162	0.0539	0.0819	0.0798	0.121	¹⁹⁵ Pt	78	117	17.83	0.162	0.0511	0.0835	0.0767	0.125
¹⁷⁶ Hf	72	104	17.57	0.169	0.0567	0.0859	0.0817	0.124	¹⁹⁶ Pt	78	118	17.83	0.162	0.0508	0.0831	0.0768	0.126
¹⁷⁷ Hf	72	105	17.59	0.170	0.0568	0.0862	0.0829	0.126	¹⁹⁸ Pt	78	120	17.87	0.161	0.0503	0.0825	0.0774	0.127
¹⁷⁸ Hf	72	106	17.64	0.166	0.0555	0.0845	0.0816	0.124	¹⁹⁷ Au	79	118	17.82	0.164	0.0512	0.0843	0.0765	0.126
¹⁷⁹ Hf	72	107	17.64	0.166	0.0551	0.0843	0.0819	0.125	¹⁹⁸ Hg	80	118	17.78	0.165	0.0513	0.0851	0.0755	0.125
¹⁸⁰ Hf	72	108	17.59	0.167	0.0558	0.0850	0.0837	0.127	¹⁹⁹ Hg	80	119	17.79	0.165	0.0512	0.0849	0.0761	0.126
¹⁸¹ Ta	73	108	17.61	0.168	0.0554	0.0855	0.0820	0.126	²⁰⁰ Hg	80	120	17.80	0.163	0.0507	0.0843	0.0759	0.126
¹⁸² W	74	108	17.51	0.171	0.0567	0.0873	0.0826	0.127	²⁰¹ Hg ^d	80	121	17.80	0.164	0.0507	0.0844	0.0767	0.128
¹⁸³ W ^d	74	109	17.58	0.171	0.0567	0.0875	0.0835	0.129	²⁰² Hg	80	122	17.83	0.162	0.0501	0.0836	0.0763	0.127
¹⁸⁴ W	74	110	17.60	0.168	0.0556	0.0859	0.0824	0.127	²⁰⁴ Hg	80	124	17.87	0.160	0.0493	0.0826	0.0764	0.128
¹⁸⁶ W	74	112	17.66	0.166	0.0544	0.0845	0.0822	0.128	²⁰³ Tl	81	122	17.80	0.164	0.0505	0.0849	0.0761	0.128
¹⁸⁵ Re ^d	75	110	17.54	0.174	0.0571	0.0887	0.0838	0.130	²⁰⁵ Tl	81	124	17.83	0.162	0.0498	0.0840	0.0762	0.129
¹⁸⁷ Re ^d	75	112	17.59	0.172	0.0564	0.0878	0.0842	0.131	²⁰⁴ Pb	82	122	17.79	0.165	0.0505	0.0856	0.0752	0.127
¹⁸⁶ Os ^h	76	110	17.65	0.170	0.0554	0.0872	0.0801	0.126	²⁰⁶ Pb	82	124	17.83	0.163	0.0497	0.0845	0.0752	0.128
¹⁸⁷ Os ^d	76	111	17.66	0.170	0.0552	0.0871	0.0807	0.127	²⁰⁷ Pb	82	125	17.85	0.162	0.0494	0.0842	0.0754	0.128
¹⁸⁸ Os	76	112	17.70	0.166	0.0539	0.0852	0.0793	0.125	²⁰⁸ Pb	82	126	17.85	0.162	0.0494	0.0841	0.0760	0.129
¹⁸⁹ Os ^d	76	113	17.68	0.168	0.0545	0.0862	0.0810	0.128	²⁰⁹ Bi	83	126	17.94	0.158	0.0474	0.0821	0.0719	0.125
¹⁹⁰ Os	76	114	17.74	0.166	0.0534	0.0849	0.0800	0.127	²³² Th ⁱ	90	142	18.70	0.137	0.0369	0.0720	0.0583	0.114
¹⁹² Os	76	116	17.74	0.164	0.0526	0.0841	0.0803	0.128	²³⁸ U ^j	92	146	18.93	0.132	0.0343	0.0695	0.0544	0.110

^a Assume $\beta = 0$ ^b Landolt-Börnstein (only rms radius) [68]^c deVries et al. [17]^d Angeli et al. [38]^e deWit et al. [34]^f Landolt-Börnstein (electron scattering) [68]^g Landolt-Börnstein (muonic X-ray) [68]^h Hoehn et al. [35]ⁱ Zumbro et al. (1986) [37]^j Zumbro et al. (1984) [36]

- [1] W. H. Bertl *et al.* (SINDRUM II Collaboration), *Eur. Phys. J. C* **47**, 337 (2006).
- [2] L. Bartoszek *et al.* (Mu2e Collaboration), *Mu2e technical design report* (2014), [arXiv:1501.05241](https://arxiv.org/abs/1501.05241) [physics.ins-det].
- [3] R. Abramishvili *et al.* (COMET Collaboration), *Prog. Theor. Exp. Phys.* **2020**, 033C01 (2020).
- [4] M. J. Lee, *Front. Phys.* **6**, 133 (2018).
- [5] M. Meucci (MEG II Collaboration), in *PoS(NuFact2021)*, 120 (2022) [arXiv:2201.08200](https://arxiv.org/abs/2201.08200) [hep-ex].
- [6] K. Arndt *et al.* (Mu3e Collaboration), *Nucl. Instrum. Methods A* **1014**, 165679 (2021), [arXiv:2009.11690](https://arxiv.org/abs/2009.11690) [physics.ins-det].
- [7] Y. Okada, K.-i. Okumura, and Y. Shimizu, *Phys. Rev. D* , 094001 (2000), [arXiv:hep-ph/9906446](https://arxiv.org/abs/hep-ph/9906446).
- [8] B. M. Dassinger, T. Feldmann, T. Mannel, and S. Turczyk, *J. High Energy Phys.* (10), 039, [arXiv:0707.0988](https://arxiv.org/abs/0707.0988) [hep-ph].
- [9] A. Matsuzaki and A. I. Sanda, *Phys. Rev. D* **77**, 073003 (2008), [arXiv:0711.0792](https://arxiv.org/abs/0711.0792) [hep-ph].
- [10] R. Kitano, M. Koike, and Y. Okada, *Phys. Rev. D* **66**, 096002 (2002).
- [11] V. Cirigliano, R. Kitano, Y. Okada, and P. Tuzon, *Phys. Rev. D* **80**, 013002 (2009).
- [12] J. Heeck, R. Szafron, and Y. Uesaka, *Phys. Rev. D* **105**, 053006 (2022).
- [13] K. Byrum *et al.* (Mu2e-II Collaboration), in *2022 Snowmass Summer Study* (2022) [arXiv:2203.07569](https://arxiv.org/abs/2203.07569) [hep-ex].
- [14] M. Aoki *et al.*, in *2022 Snowmass Summer Study* (2022) [arXiv:2203.08278](https://arxiv.org/abs/2203.08278) [hep-ex].
- [15] R. Barrett, *Phys. Lett. B* **33**, 388 (1970).
- [16] S. Davidson, Y. Kuno, and A. Saporta, *Eur. Phys. J. C* **78** (2018).
- [17] H. De Vries, C. De Jager, and C. De Vries, *At. Data Nucl. Data Tables* **36**, 495 (1987).
- [18] W. C. Haxton, E. Rule, K. McElvain, and M. J. Ramsey-Musolf, *Phys. Rev. C* **107**, 035504 (2023), [arXiv:2208.07945](https://arxiv.org/abs/2208.07945) [nucl-th].
- [19] S. Davidson and B. Echenard, *Eur. Phys. J. C* **82**, 836 (2022), [arXiv:2204.00564](https://arxiv.org/abs/2204.00564) [hep-ph].
- [20] D. F. Measday, *Phys. Rep.* **354**, 243 (2001).
- [21] S. Weinberg and G. Feinberg, *Phys. Rev. Lett.* **3**, 111 (1959).
- [22] P. H. Stelson and L. Grodzins, *Nucl. Data Sheets A* **1** (1965).
- [23] S.-G. Zhou, J. Meng, P. Ring, and E.-G. Zhao, *Phys. Rev. C* **82**, 011301 (2010), [arXiv:0909.1600](https://arxiv.org/abs/0909.1600) [nucl-th].
- [24] L. Li, J. Meng, P. Ring, E.-G. Zhao, and S.-G. Zhou, *Phys. Rev. C* **85**, 024312 (2012), [arXiv:1202.0070](https://arxiv.org/abs/1202.0070) [nucl-th].
- [25] K. Zhang *et al.*, *At. Data Nucl. Data Tables* **144**, 101488 (2022).
- [26] C. Pan *et al.*, *Phys. Rev. C* **106**, 014316 (2022).
- [27] P. Pyykko, *Mol. Phys.* **106**, 1965 (2008).
- [28] D. Dehnhard, *Phys. Lett. B* **38**, 389 (1972).
- [29] J. H. Heisenberg, J. S. McCarthy, I. Sick, and M. R. Yearian, *Nucl. Phys. A* **164**, 340 (1971).
- [30] E. R. Macagno, S. Bernow, S. C. Cheng, S. Devons, I. Duerdoth, D. Hitlin, J. W. Kast, W. Y. Lee, J. Rainwater, C. S. Wu, and R. C. Barrett, *Phys. Rev. C* **1**, 1202 (1970).
- [31] M. Rose, *Phys. Rev.* **82**, 389 (1951).
- [32] A. Bartolotta and M. J. Ramsey-Musolf, *Phys. Rev. C* **98**, 015208 (2018), [arXiv:1710.02129](https://arxiv.org/abs/1710.02129) [hep-ph].
- [33] G. Fricke, C. Bernhardt, K. Heilig, L. Schaller, L. Schellenberg, E. SHERA, and C. Dejager, *At. Data Nucl. Data Tables* **60**, 177 (1995).
- [34] S. De Wit, G. Backenstoss, C. Daum, J. Sens, and H. Acker, *Nucl. Phys.* **87**, 657 (1966).
- [35] M. V. Hoehn, E. B. SHERA, H. D. Wohlfahrt, Y. Yamazaki, R. M. Steffen, and R. K. Sheline, *Phys. Rev. C* **24**, 1667 (1981).
- [36] J. D. Zumbro, E. B. SHERA, Y. Tanaka, C. E. Bemis, R. A. Naumann, M. V. Hoehn, W. Reuter, and R. M. Steffen, *Phys. Rev. Lett.* **53**, 1888 (1984).
- [37] J. D. Zumbro, R. A. Naumann, M. V. Hoehn, W. Reuter, E. B. SHERA, C. E. Bemis, and Y. Tanaka, *Phys. Lett. B* **167**, 383 (1986).
- [38] I. Angeli and K. Marinova, *At. Data Nucl. Data Tables* **99**, 69 (2013).
- [39] P. Möller, A. Sierk, T. Ichikawa, and H. Sagawa, *At. Data Nucl. Data Tables* **109-110**, 1 (2016).
- [40] M. Ardu, S. Davidson, and S. Lavignac, *J. High Energy Phys.* (11), 101, [arXiv:2308.16897](https://arxiv.org/abs/2308.16897) [hep-ph].
- [41] A. Lagarrigue and C. Peyrou, *J. Phys. Radium* **12**, 848 (1951).
- [42] F. B. Harrison, J. W. Keuffel, and G. T. Reynolds, *Phys. Rev.* **83**, 680 (1951).
- [43] J. Steinberger and H. B. Wolfe, *Phys. Rev.* **100**, 1490 (1955).
- [44] T. Suzuki, D. F. Measday, and J. P. Roalsvig, *Phys. Rev. C* **35**, 2212 (1987).
- [45] D. F. Measday, T. J. Stocki, B. A. Mofteh, and H. Tam, *Phys. Rev. C* **76**, 035504 (2007).
- [46] J. A. Wheeler, *Rev. Mod. Phys.* **21**, 133 (1949).
- [47] W. Honecker *et al.* (SINDRUM II Collaboration), *Phys. Rev. Lett.* **76**, 200 (1996).
- [48] D. Sard, K. M. Crowe, and H. Kruger, *Phys. Rev.* **121**, 619 (1961).
- [49] M. Conversi, L. di Lella, A. Egidi, C. Rubbia, and M. Toller, *Phys. Rev.* **122**, 687 (1961).
- [50] G. Conforto, M. Conversi, L. di Lella, G. Penso, C. Rubbia, and M. Toller, *Il Nuovo Cimento* **26**, 261 (1962).
- [51] J. H. Bartley, H. Davies, H. Muirhead, and T. Woodhead, *Phys. Lett.* **16**, 187 (1965).
- [52] D. A. Bryman, M. Blecher, K. Gotow, and R. J. Powers, *Phys. Rev. Lett.* **28**, 1469 (1972).
- [53] A. Badertscher *et al.*, *Phys. Rev. Lett.* **39**, 1385 (1977).
- [54] A. Badertscher *et al.*, *Nucl. Phys. A* **377**, 406 (1982).
- [55] S. Ahmad *et al.*, *Phys. Rev. D* **38**, 2102 (1988).
- [56] C. Dohmen *et al.* (SINDRUM II Collaboration), *Phys. Lett. B* **317**, 631 (1993).
- [57] S. Eggli, *Such nach der leptonflavourverletzenden μ -Konversion: μ -Ti \rightarrow e-Ti*, Ph.D. thesis, Philosophischen Fakultät II der Universität Zürich (1995).
- [58] A. Crivellin, S. Davidson, G. M. Pruna, and A. Signer, *J. High Energy Phys.* **2017** (5).
- [59] R. Szafron, *Acta Phys. Pol. B* **48**, 2183 (2017).
- [60] A. Czarnecki, X. Garcia i Tormo, and W. J. Marciano, *Phys. Rev. D* **84**, 013006 (2011).
- [61] R. Szafron and A. Czarnecki, *Phys. Lett. B* **753**, 61 (2016), [arXiv:1505.05237](https://arxiv.org/abs/1505.05237) [hep-ph].
- [62] Mu2e Collaboration, *Universe* **9** (2023),

- [arXiv:2210.11380 \[hep-ex\]](#).
- [63] M. Röhrken (Mu2e Collaboration), in *PoS(ICHEP2016)*, Vol. 282 (2017) p. 783.
- [64] J. Cobb *et al.* (Brookhaven-CERN-Syracuse-Yale Collaboration), *Nucl. Instrum. Methods* **140**, 413 (1977).
- [65] S. Davidson, Y. Kuno, and M. Yamanaka, *Phys. Lett. B* **790**, 380–388 (2019).
- [66] V. Cirigliano, S. Davidson, and Y. Kuno, *Phys. Lett. B* **771**, 242 (2017).
- [67] K. Fuyuto and E. Mereghetti, ALP contributions to $\mu \rightarrow e$ conversion (2023), [arXiv:2307.13076 \[hep-ph\]](#).
- [68] G. Fricke and K. Heilig, Nuclear charge radii, in *Landolt-Börnstein: Numerical Data and Functional Relationships in Science and Technology*, Group I: Elementary Particles, Nuclei and Atoms, Vol. 20, edited by H. Schopper (Springer, 2004).